Zonal large-eddy simulation of a tip leakage flow

Jérôme Boudet,[1] Joëlle Caro,[1] Bo Li,[1] Emmanuel Jondeau[1] and Marc C Jacob[2]

Abstract

The flow induced by the clearance between the tip of an isolated airfoil and an end-plate is investigated numerically, using a zonal approach with large-eddy simulation in the region of interest. The results are analyzed in comparison with available experimental data, presented in a companion paper. The incoming boundary layer and the pressure distribution around the blade are evaluated. The description of the inflow-jet deviation, with an averaged approach, enables to represent the proper loading on the airfoil. Also, particular attention is paid to the powerful tip-leakage vortex. The vortex characteristics are investigated using specific functions to locate its center and quantify its width. Overall, good results are obtained for the flow statistics and spectra. Furthermore, a very good description of the far-field pressure is achieved using the acoustic analogy, and the results confirm that the tip-flow essentially radiates in the central frequency range (0.7 kHz, 7 kHz).

Introduction

In the context of air-traffic growth, the international regulations on aircrafts are regularly enforced to limit the pollutant emissions and noise. These issues particularly concern the internal aerodynamics of the turbojet engines. Indeed, the secondary flow structures[1] that develop within the blade passages induce energy losses and participate to noise emission. Among the secondary flow structures, the tip-leakage vortex (TLV) is a powerful feature, generated from the blade-tip clearance and developing in the blade passage.

[1]Univ Lyon, Ecole Centrale de Lyon, Université Claude Bernard Lyon I, CNRS, LMFA, Ecully, France
[2]DAEP, ISAE-SupAéro, Toulouse, France

Corresponding author:
J Boudet, LMFA, UMR CNRS 5509 – Ecole Centrale de Lyon, 36 avenue Guy de Collongue, F-69134 Ecully Cedex, France.
Email: jerome.boudet@ec-lyon.fr

Examples are numerous of successful averaged (Reynolds-averaged Navier–Stokes (RANS)) simulations of the TLV. Among those, we can cite the early work of Storer and Cumpsty.[2] Nowadays, such simulations are commonly used to design the flow path in turbomachines. However, the RANS simulations are not able to reproduce the broadband noise emission mechanisms associated with the turbulent dynamics. Moreover, recent studies have shown that the TLV can develop large-scale oscillations, referred to as "vortex wandering", that can contribute also the noise emissions. RANS simulations do not capture this kind of natural unsteadiness. These arguments motivate the use of large-eddy simulation (LES), which relies on a direct description of the largest turbulent eddies. As such, LES is expected to provide a detailed representation of the TLV dynamics. A typical illustration of a LES simulation in the context of turbomachines is provided by Hah,[3] who employed this strategy on the NASA rotor 37. You et al.[4,5] also employed LES to investigate the flow in a cascade configuration, with particular attention to the TLV. You et al. obtained very good comparisons with the experiment, in particular for the flow spectra, where a broad peak corresponding to the vortex-wandering phenomenon was observed. More recently, Boudet et al.[6] presented a zonal RANS/LES simulation of a laboratory-scale fan. The region around the tip of the blade was described with full-LES, while RANS was used at lower radii in order to limit the computational cost. The TLV wandering has been observed again in this rotating configuration, and its spectral footprint confirmed by the experimental data.

In the present paper, an isolated airfoil configuration with tip leakage is considered. The corresponding experiment is presented in a companion paper from Jacob et al.[7] A major advantage of this simplified configuration, with respect to more complex configurations mentioned above, lies in the acoustic characterization. In particular, experimental sound measurements are available in anechoic conditions. The present paper focuses on a zonal RANS/LES simulation of this configuration, with a full-LES description of the tip region. The objective is essentially to evaluate the capabilities of the simulation with respect to the experimental data, on both the aerodynamic and acoustic point of views. This is also a first opportunity to extend the analysis beyond the capabilities of the experiment, typically in the higher frequency range. In the Simulation set-up section, the set-up of the simulation is presented. In the Results and discussion section, results are presented in comparison with experimental data, and the analysis is developed. Finally, conclusions are drawn in the last section.

Simulation set-up

A sketch of the configuration is presented in Figure 1: an isolated airfoil is set in the potential core of a rectangular jet, and enclosed between two end-plates. A clearance is arranged between the airfoil and the lower end-plate. Various experimental results are available on this configuration, as reported in the companion paper by Jacob et al.[7] The blade chord–length is $c = 0.2$ m. In the present numerical study, the following conditions are selected: $U_0 = 70$ m/s and $h = 0.01$ m. The chord-based Reynolds number is about 9.3×10^5, and the Mach number is 0.2.

Two experimental campaigns have been carried out on this configuration. The first campaign is presented by Jacob et al.[8] The angle of attack was set to $\theta = 15°$ ($\pm 0.5°$). Several years later, the rig has been re-installed with some adaptations, including a reduction of the incoming boundary layer thickness. A second test campaign has been carried out, presented in the companion paper of Jacob et al.[7] During this second campaign, the angle of attack had to be adjusted to $\theta = 16.5°$ ($\pm 0.5°$), in order recover the same pressure distribution
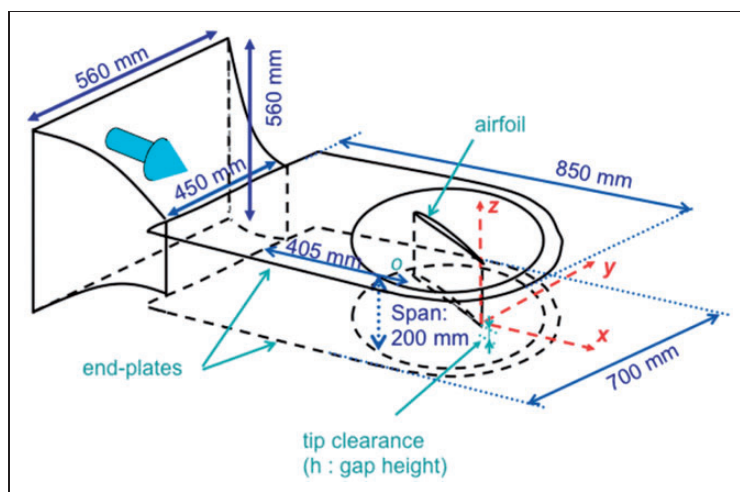
Figure 1. Sketch of the configuration. The axis origin is on the airfoil tip trailing-edge.

at mid-span as for the first campaign. The simulation has been initiated simultaneously with the second experimental campaign, with the original angle of attack of $\theta = 15°$, and a thin incoming boundary layer. The numerical results will be compared with the second experimental campaign. The consistency of the experiment and the simulation will be checked on the incoming boundary layer thickness and the pressure distribution at mid-span, considered as representative of the flow conditions.

Zonal simulation strategy

In the present configuration, the airfoil deviates the jet, which in turn influences the loading of the airfoil. As shown by Moreau et al.,[9] this feedback has to be taken into account in simulations, so that proper loading can be predicted. It is not possible to assume the inflow to be uniform, and the interaction between the airfoil and the jet must be represented.

The present work is focused on the tip leakage flow and noise, and LES is employed to provide a detailed description of the turbulent dynamics in this region. But a precise description of the jet shear-layers is not the purpose of the present paper. Consequently, LES is circumscribed in the region of the jet around the tip leakage and in the incoming boundary layer (on the lower end-plate). RANS is used in the rest of the domain in order to alleviate the computational needs of the simulation. This approach is inspired by Winkler et al.,[10] who simulated a spanwise section of an isolated airfoil in a jet. These authors carried out a preliminary RANS simulation over the whole domain, in order to extract the boundary conditions for a local LES simulation. In contrast, in the present case, the LES and RANS zones are disjointed and fully coupled. Such an approach can be referred to as zonal RANS/LES. Moreover, the tip-clearance flow considered here is certainly influenced by the incoming boundary layer on the lower end-plate, whose thickness is of the same order as the tip-gap height (h). Consequently, this boundary layer has to be described by LES.

The LES/RANS coupling is ensured by a smooth evolution of the eddy viscosity, from the LES subgrid-scale viscosity to the RANS turbulent viscosity. The eddy viscosity is calculated
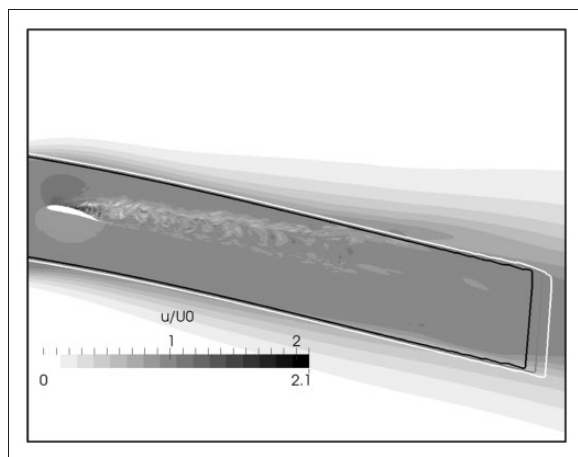
Figure 2. Zonal decomposition around the airfoil tip region. The black, grey and white lines enclosing the airfoil correspond respectively to $\beta = 0.1$, $\beta = 0.5$ and $\beta = 0.9$.

as: $\mu_{mod} = (1 - \beta(x, y, z))\mu_{sgs} + \beta(x, y, z)\mu_t$, where $\beta(x, y, z)$ is the prescribed zonal coefficient. The details of the implementation are presented in Boudet et al.,[6] where this approach is used for a rotor tip-flow simulation. The prescription of β used in the present configuration is illustrated in Figure 2, where the iso-lines $\beta = 0.1$, 0.5 and 0.9 are plotted over an instantaneous flow field in an x–y plane, and enable to locate the interface between the LES and RANS zones. As mentioned above, the LES is circumscribed in the incoming boundary layer and around the tip-clearance region. In the spanwise direction, the LES region extends up to $z = 4h$ (where $\beta = 0.5$). The same models as in Boudet et al.[6] are employed. The shear-improved Smagorinsky model[11] is used to evaluate the LES subgrid-scale viscosity μ_{sgs}, with exponential averaging for the mean-shear estimate (cut-off frequency: $1.8U_0/c$). The $k - \omega$ model of Wilcox[12] provides the RANS turbulent viscosity μ_t.

Compared with the previous work of You et al.,[4,5] the present numerical study essentially brings two elements. First, the zonal approach: the LES is focused on the region of interest in order to reduce the computational cost, which is a crucial issue for the generalization of LES simulations. This zonal methodology will be evaluated by comparison with the experiment. Second, the acoustics is considered in the present configuration, trying to shed new light on the relationship with the tip leakage turbulent dynamics.

Numerical methods, parameters and grid

The flow simulation (CFD) has been performed with the in-house solver *Turb'Flow*.[6,13] This solver uses a cell-vertex finite-volume discretization on multi-block structured grids, and it is particularly dedicated to turbomachine applications. In the present simulation, the inviscid fluxes are interpolated with a four-point centered scheme, with a fourth-order artificial viscosity term inspired by Jameson.[14] The artificial viscosity coefficient is set to 0.003 on the end-plate in the clearance, increases smoothly up to 0.03 in the outer part of the LES zone and up to 0.3 in the RANS region. The influence of this coefficient has been previously tested in Boudet et al.,[13] in LES simulations of a flat-plate boundary layer. The viscous fluxes
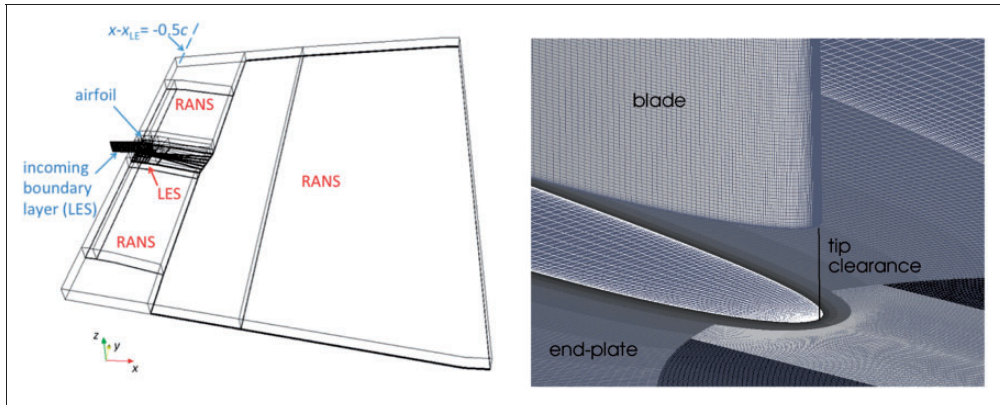
Figure 3. *Left*: global view of the computational domain blocks. *Right*: close-up view of the grid around the tip-clearance, in the leading edge region.

are interpolated with a two-point centered scheme. The temporal discretization relies on a three-step Runge-Kutta scheme, with time-step: $5.6 \times 10^{-6} \, c/U_o$.

A global view of the computational domain is presented in Figure 3 (left). It extends over 29c/37c/1c in the streamwise/lateral/spanwise directions. A close-up view of the grid around the tip-clearance, in the leading-edge region, is shown in Figure 3 (right). The total grid is composed of 524 structured blocks, and the total number of points is about 150×10^6. In the LES zones, the cell dimensions at the walls are: $\Delta x^+ < 80$ (stream-wise), $\Delta y^+ < 1.5$ (wall-normal) and $\Delta z^+ < 30$ (cross-stream), in wall units. This is consistent with standard practices of wall-resolved LES, and with previous boundary-layer tests.[13]

Within the jet, the complete development of the lower end-plate incoming boundary layer is simulated by LES over a limited lateral length (about the boundary layer thickness) and repeated periodically in the *y*-direction, up to $x - x_{LE} = -0.5c$ (see Figure 3(left)). Uniform density and velocity profiles are imposed at the boundary layer inlet, and the transition to turbulence is tripped by a source term.[13] At the inflow boundary of the RANS zone outside the jet, density and a minimal velocity (=1 m/s) are imposed. A no-slip adiabatic condition is set on the walls (blade and lower end-plate) and symmetry on the upper end-plate. The side boundaries are tilted outward in order to impose an inflow condition. Static pressure is imposed on the outlet, with a buffer layer and a semi-non-reflecting condition (see Boudet et al.[6] for details).

Starting from a preliminary RANS solution, the present simulation has run during six flow-through periods (c/U_o), then the statistics have been acquired over an additional six flow-through periods.

The CFD methods above are dedicated to the flow simulation, and are not specifically adapted to acoustic propagation. Consequently, the propagation to the far-field is ensured by the Ffowcs-Williams and Hawkings[15] acoustic analogy. It is implemented in the *Turb'AcAn* solver, which follows the formulation of Casalino,[16] but here run a posteriori from the CFD results. *Turb'AcAn* has been validated on academic test-cases proposed by Casalino, and has also been compared to a linearized Euler equation solver in Jacob et al.[17] In the present study, the propagation is in a medium that is assumed at rest, neglecting the influence of the jet. The volume sources are neglected, given the low Mach number (0.2 at the inflow), and the surface integration is carried out on the blade surface. A free-field
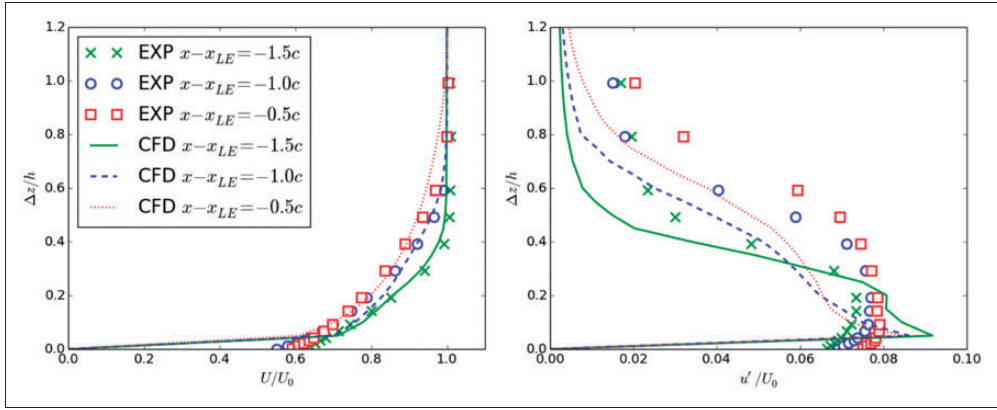
Figure 4. Velocity profiles in the incoming boundary layer, at three different axial positions $x–x_{LE} = -1.5c$, $-1.0c$ and $-0.5c$. *Left*: mean velocity. *Right*: fluctuating velocity. The span-wise distance (Δz) is measured from the end-plate.

propagation is supposed, neglecting the reflections on the end-plates supporting the airfoil. The far-field computation relies on the six flow-through periods acquired from the CFD simulation, with a sampling period of $1.68\times10^{-2}c/U_o$.

Results and discussion

In this section, the results of the simulation are compared to available experimental data, and the analysis of the flow and the acoustics is developed further.

Incoming boundary layer

The thickness of the boundary layer on the lower end-plate is of the same order as the tip-clearance height. Consequently, this boundary layer has certainly an influence on the leakage flow. This is why the present simulation has been configured to represent this boundary layer with full LES, in order to describe both the mean flow and the turbulence characteristics. The development of the boundary layer can be compared to hot-wire measurements at three axial positions upstream of the airfoil leading edge: $x–x_{LE} = -1.5c$, $-1.0c$ and $-0.5c$. The results are plotted in Figure 4, for both the mean velocity and the root mean squared (rms) fluctuations. Considering the mean velocity, one can verify here that the boundary layer thickness is slightly lower than the tip-gap height (h). A very good agreement is achieved between the experiment and the simulation, at the three positions. The thickness of the boundary layer and its stream-wise evolution are properly simulated. Concerning the fluctuations, a good agreement is obtained between the CFD and the experiment at $x–x_{LE} = -1.5c$, within the boundary layer. In the free flow ($\Delta z/h > 0.6$), there is some turbulence in the experiment ($u'/U_0 \approx 1.7\%$), but it is neglected in the simulation. At the downstream sections ($x–x_{LE} = -1.0c$ and $-0.5c$), the boundary layer thickness appears well described, but the turbulence intensity in the boundary layer is underestimated. Furthermore, the CFD results present the classical peak of fluctuations near the wall (refer, for example, to DeGraaf and Eaton[18]), but not the experiment. These differences may be explained by the different history of the boundary layer: in the experiment, it comes from the wind tunnel through the
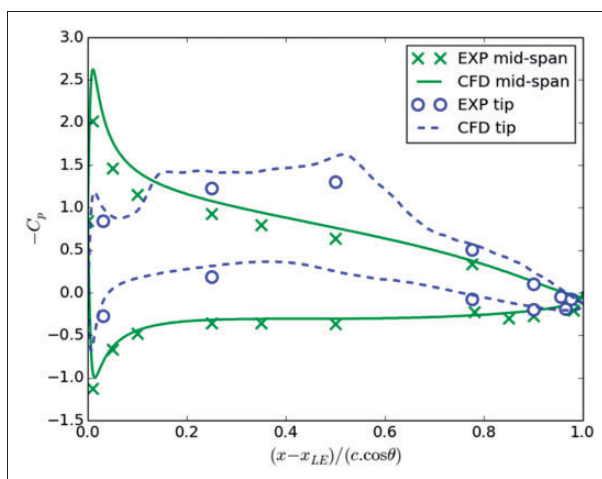
Figure 5. Mean pressure coefficient at mid-span ($z = 0.1$ m), and close to the tip ($z = 0.1\,h$).

nozzle, whereas in the CFD it is a flat plate boundary layer. The longer development of the boundary layer in the experiment may explain the smoothing of the fluctuation peak. Furthermore, the description of this peak with hot-wire is known as difficult (see again DeGraaf and Eaton[18]). Overall, the description of the incoming boundary layer by the CFD is considered satisfactory for the simulation of the downstream tip leakage flow.

Mean pressure distribution

The mean pressure distribution around the blade is presented in Figure 5, at mid-span ($z = 0.1$ m) and close to the tip ($z = 0.1\,h$). The results at mid-span are considered first. A fairly good agreement is achieved between the measurements and the CFD, given the uncertainty in the experimental angle of attack. The gradients are well reproduced by the simulation. In the tip region, the pressure difference between the two sides of the blade is globally reduced. This indicates a reduction of the blade loading, because of the tip leakage. A low-pressure hump is observed on the suction side, due to the jet-like flow leaving the gap in this region (cf. Jacob et al.[8]), where the TLV starts to develop. A fairly good agreement is also observed in the tip region, concerning the blade loading, the gradients, and the location of the TLV.

Some additional comments can be made about the influence of the jet deviation. Previous RANS studies (see for example Boudet et al.[19]), which assumed the airfoil in a homogeneous inflow, had to set the angle of attack to $\theta = 7°$ (instead of $\theta = 15°$ in the first experimental campaign) in order to obtain a proper $-C_p$ distribution at mid-span. Here, the jet is simulated, and a correct $-C_p$ distribution is obtained with an angle of attack ($\theta = 15°$) similar to the experimental value ($\theta = 16.5°$ in the second experimental campaign). This demonstrates the influence of the jet deviation in the present configuration.

Tip-leakage vortex

A visualization of the mean TLV is presented in Figure 6, where contours of normalized mean axial vorticity are shown on four cross-stream planes near the trailing edge.
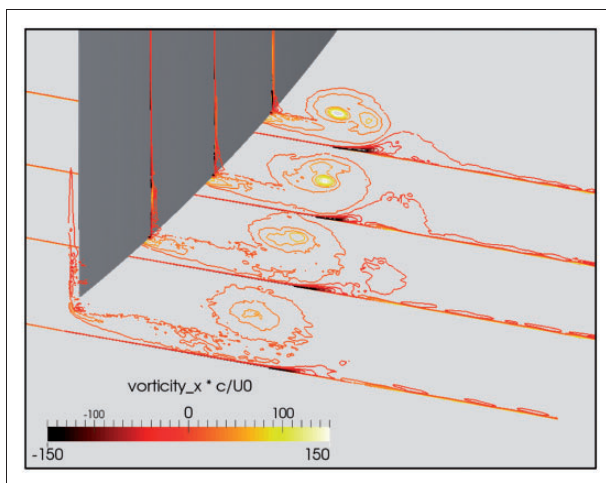
Figure 6. Contours of non-dimensional mean axial vorticity on four cross-stream planes near the trailing edge of the airfoil.

The concentric contours of high vorticity indicate the TLV. It progressively deviates from the suction surface and its vorticity diffuses, confirming a trend evidenced in the experiment.[7] High levels of vorticity are also observed in the leakage flow below the airfoil.

The mean velocity components are extracted in a cross-stream plane (constant x), 2 mm downstream of the airfoil trailing edge, and compared to particle image velocimetry (PIV) measurements. The CFD results are interpolated on the PIV grid, and the same post-processing is employed. The results are plotted in Figure 7. The flow field is viewed from downstream, and the blade wake is around $y = 0$ mm and $z \geq 0$ mm. The PIV results are not available in a rectangular region (about $0 \leq y \leq 20$ mm and $z \geq 0$ mm) around the wake of the airfoil, because of laser reflections, and the velocity is prescribed to zero.

The TLV roll-off is clearly visible on these figures, through the velocity vector field. The distribution of the cross-stream components of velocity is governed by this vortex. High values of V (horizontal component) are induced near the lower plate in the continuation of the leakage through the clearance. Negative values are observed above, because of the recirculation. Concerning W (vertical component), the recirculation causes high positive and negative values, respectively, on the right-hand side and left-hand side of the vortex. A very good agreement is achieved between the experiment and the simulation, regarding both the topology of the flow and the magnitudes of the velocity. The amplitude of the cross-stream components of velocity is remarkable: about U_0. This plane is downstream of the blade, and there is no more leakage, but the TLV is still particularly intense. Also, the position and the size of the TLV seem to be well reproduced by the simulation.

A more precise analysis of the vortex characteristics (position and size) can be achieved by the extraction of appropriate quantities. Here, the analysis will use the vortex identification functions Γ_1 and Γ_2 introduced by Graftieaux et al.[20] and also employed in the experimental companion paper.[7] These functions are plotted in Figure 8, for both the PIV and the CFD
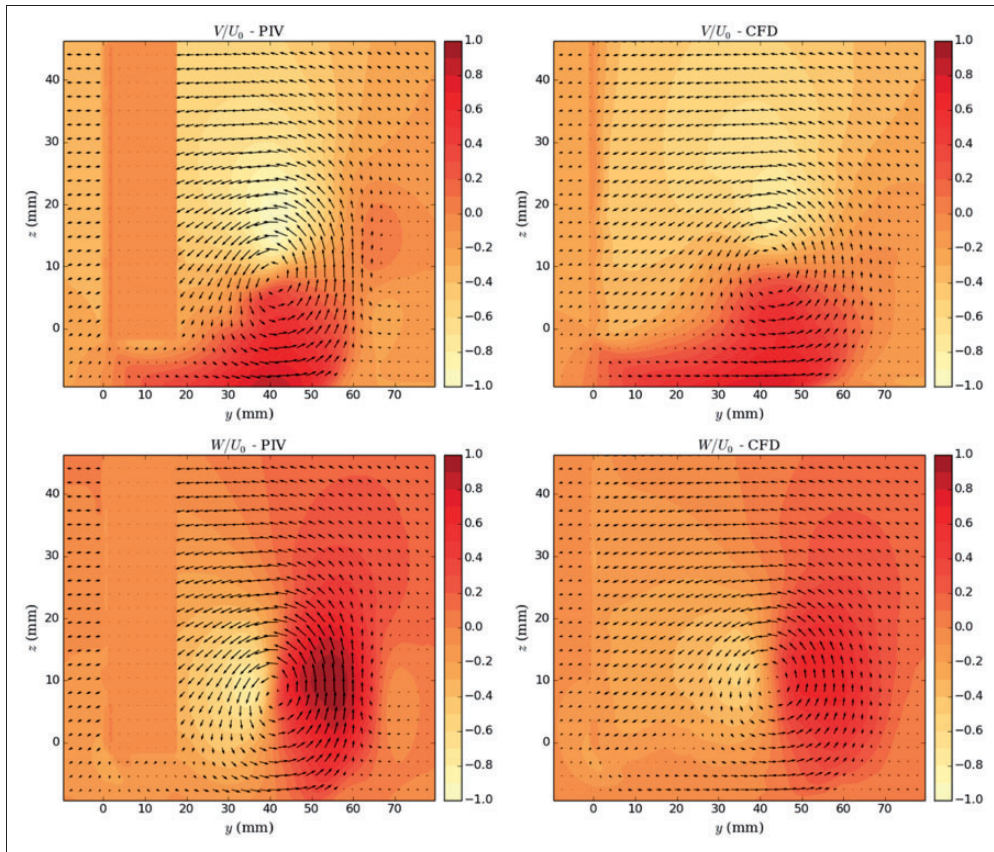
Figure 7. Mean velocity vectors and component contours (top: horizontal component V/U_0, bottom: span-wise component W/U_0). Left: PIV measurements, right: CFD.

mean flows, on the same plane, 2 mm downstream of the trailing edge. Both functions are normalized.

The extrema of Γ_1 locate the centers of the vortices, with positive (resp. negative) values for anticlockwise (resp. clockwise) rotation. In Figure 8, a very good agreement is observed between the PIV and CFD distributions of Γ_1. The center of the TLV is clearly detected by $\Gamma_1 \approx 1$ in a narrow region. The vortex center is slightly more distant, in both y and z directions, in the CFD than in the PIV. Also, a counter-rotating vortex ($\Gamma_1 \approx -1$) is visible aside the TLV in the PIV, around $y = 70$ mm and $z = 10$ mm. In the CFD, a region with $\Gamma_1 \le 0$ is also visible, but less clearly than in the PIV.

The distribution of Γ_2 indicates the extent of the vortices, with again positive (resp. negative) values for anticlockwise (resp. clockwise) rotation. In Figure 8, a good agreement is observed between the PIV and CFD distributions. The size of the TLV is very similar in both the experiment and the simulation, slightly larger in the CFD. The elliptic area with $\Gamma_2 \le 0$ on the right-hand side of the TLV, corresponding to the counter-rotating vortex, is clearly defined in the PIV. The region is more irregular in the CFD, probably because of imperfect statistic convergence.
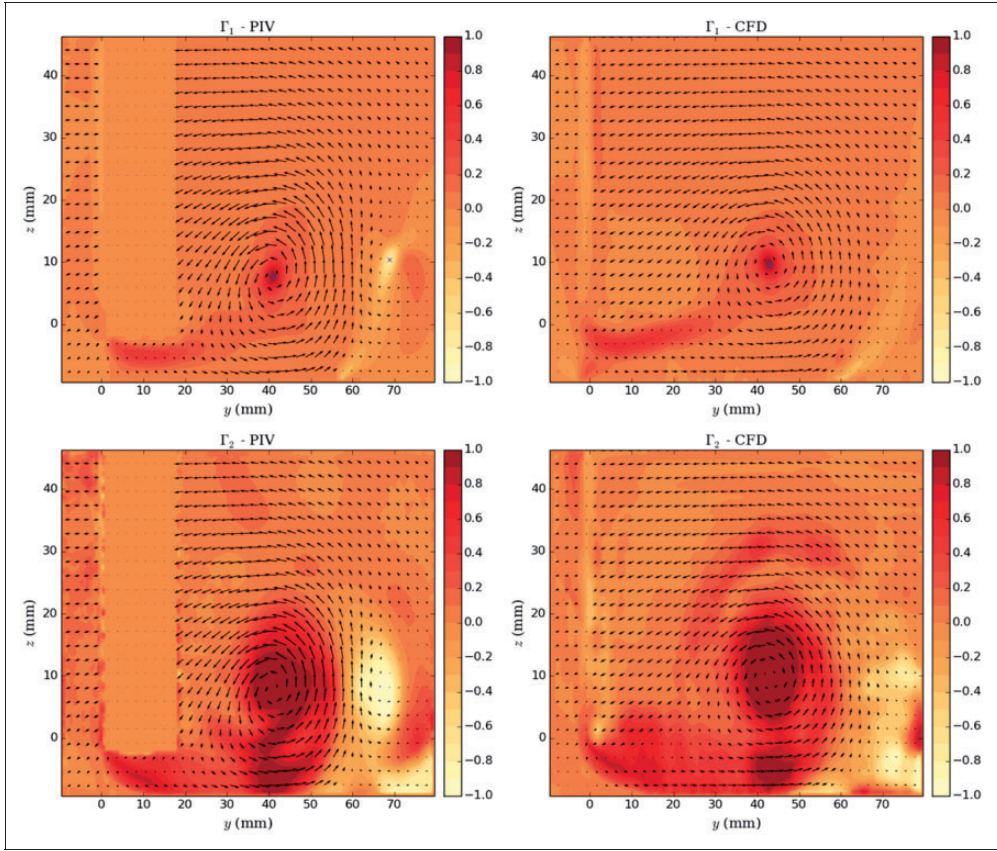
Figure 8. Vortex identification functions (top: Γ_1, bottom: Γ_2). Left: experiment (PIV), right: CFD.

Overall, the comparisons of the distributions of Γ_1 and Γ_2 show a very good agreement between the experiment and the CFD mean flows, concerning both the location and the size of the TLV.

The trajectory of the mean TLV center, located with the maximum of Γ_1 for different axial positions (constant x), is plotted in Figure 9. A very good agreement is obtained between the experiment and the simulation.

Velocity and pressure fluctuations

A major interest of LES is to provide a description of the velocity fluctuations induced by the largest (and most energetic) turbulent eddies. This description is here compared to the experiment, considering the rms velocity fluctuations on the plane 2 mm downstream of the trailing edge. The results are plotted in Figure 10, for the cross-stream horizontal and vertical components of velocity. High velocity fluctuations are observed around the TLV center, where the mean velocity gradients are strong. Intense fluctuations are also observed in the continuation of the leakage flow, near the end-plate ($0\,\text{mm} \leq y \leq 50\,\text{mm}$, $z \leq 0\,\text{mm}$). This is also a region of intense gradients, since it is just downstream the jet flow through the
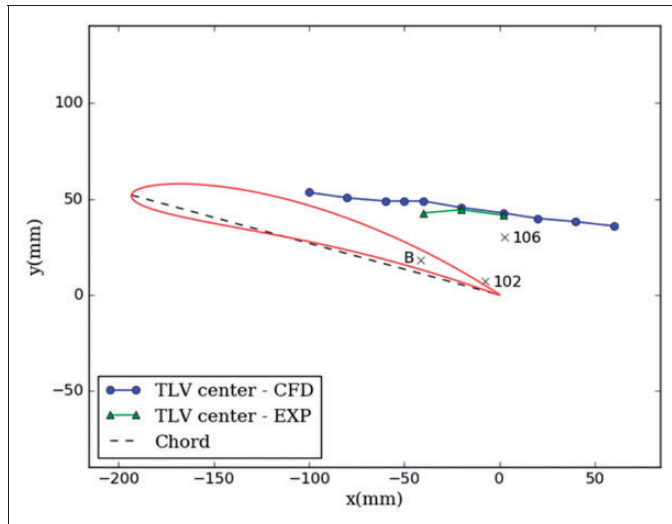
Figure 9. Mean TLV center trajectory, and probe locations. Probe 'B' is on the blade tip, whereas probes '102' and '106' are at $z = -h/2$.

tip-clearance. High velocity fluctuations are also observed on the right-hand side of the TLV, near the counter-rotating vortex. Overall, the CFD results are in good agreement with the experiment, but are slightly more diffused, considering the lower intensity in the vortex core and the wider spreading of the fluctuations around the TLV. This is a classical issue with numerical results, and it is particularly moderate in the present case. Finally, a region of intense horizontal fluctuations (v') is observed near the end-plate, between the TLV and the counter-rotating vortex (i.e. $y \approx 60$ mm and $z \leq 0$ mm). This region corresponds to the scraping of the end-plate boundary layer, and the associate turbulence, by the TLV. This is a particularly interesting phenomenon, since the turbulent characteristics of the incoming boundary layer will be transported around the TLV and could affect the noise emission around the blade tip.

The analysis will now focus on the spectral content in the tip region around the trailing edge. Three probes are selected in this region, and represented in Figure 9. First, a pressure probe on the blade tip, labeled 'B', is considered. The experimental and numerical spectra are presented in Figure 11. For this probe, the experimental data come from the first campaign,[8] with a thicker incoming boundary layer, while the rest of the paper uses experimental results from the second campaign. The CFD globally over-estimates the levels, by some decibels, but the shape of the spectrum is wall captured. The turbulent dynamics in the gap is characterized by a spectrum hump around 1 kHz. This feature is well described by the simulation: both the central frequency and the amplitude of the hump are predicted. Moreover, the spectrum slope at higher frequencies is also well reproduced by the simulation. Next, the velocity probes 102 and 106 are considered. The power spectral densities of w/U_0 at these points are plotted in Figure 12. Probe 106 is the closest to the TLV center, and experimental data (Laser Doppler Velocimetry[7]) are available at this point. Only lower frequencies are accessible from the experiment, while the CFD essentially describes higher frequencies. However, a good match is obtained in the intermediate frequency
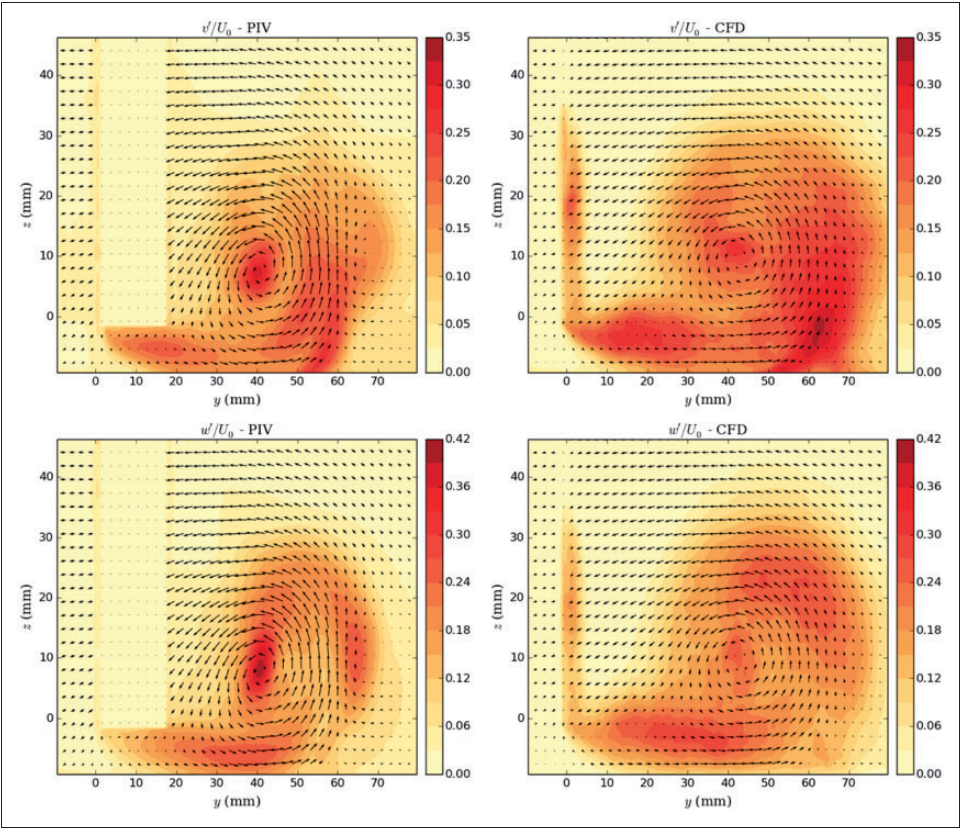
Figure 10. Fluctuating velocities (top: v'/U_0, bottom: w'/U_0). *Left*: experiment, *right*: CFD.
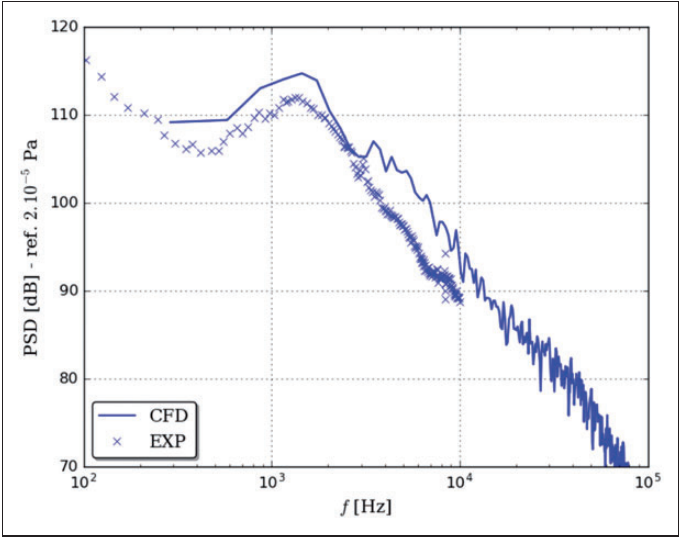

Figure 11. Pressure spectrum on the blade tip (at probe 'B', introduced in Figure 9).
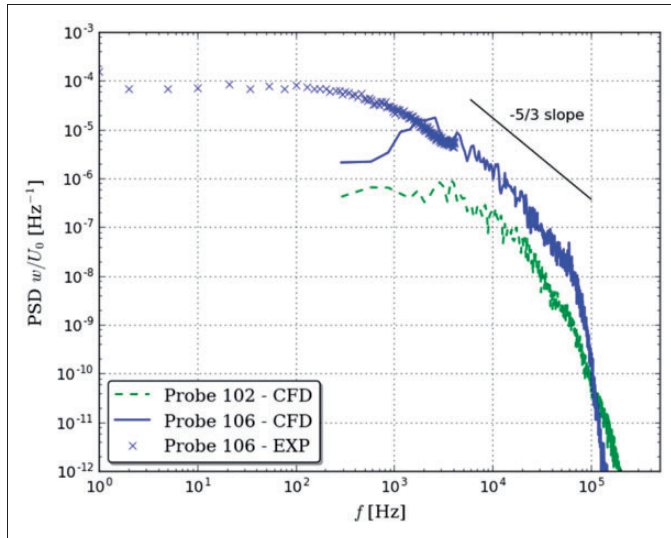
Figure 12. Power spectral density of w/U_0 at two positions between the trailing edge and the TLV (cf. probe locations in Figure 9).

range (around 2–4 kHz): both the levels and the spectrum slope are well predicted by the simulation. This frequency range is remarkable because it can be associated with the TLV. Indeed, a characteristic frequency of the TLV can be defined from Figures 7 and 8 (Γ_2): the characteristic velocity is U_0, and the characteristic diameter is about 20 mm. This yields a characteristic frequency of order 3 kHz, for a Strouhal number of unity. This is slightly above the frequency of the hump observed on the pressure spectrum in the tip region in Figure 11. Furthermore, this characteristic frequency (3 kHz) lies in the range of frequencies where the measured tip-clearance noise is highest with respect to background noise (cf. Jacob et al.[7]) At probe 106, for frequencies below 2 kHz, the numerical spectrum is damped and diverge from the experiment. This may be caused by the limited spatial extension of the LES zone (cf. Figure 2): the largest eddies cannot be described by the simulation. There is no such limitation in the experiment, which also includes the unsteadiness of the jet. Finally, probe 102 is the closest to the blade tip. The energy is lower at this point, but the spectrum shape is very similar to the probe inside the TLV, with a broad range of frequencies. High frequency eddies are probably transported to this point by the blade boundary layers. The spectral distribution at this point is particularly interesting because the proximity of the tip trailing edge, as a geometric singularity, supports the conversion of the turbulent fluctuations into acoustics.

Acoustics

Finally, the far-field pressure at 2 m from the suction side of the airfoil, in the direction perpendicular to the inflow (y-direction), is considered. The experimental and numerical results are plotted in Figure 13. Two levels of averaging of the CFD spectrum are presented: no average (i.e. the spectrum is calculated on the total time-sample), and with a nine blocks average (i.e. the numerical time-sample is split into 9 pieces, with 50% overlap, and the
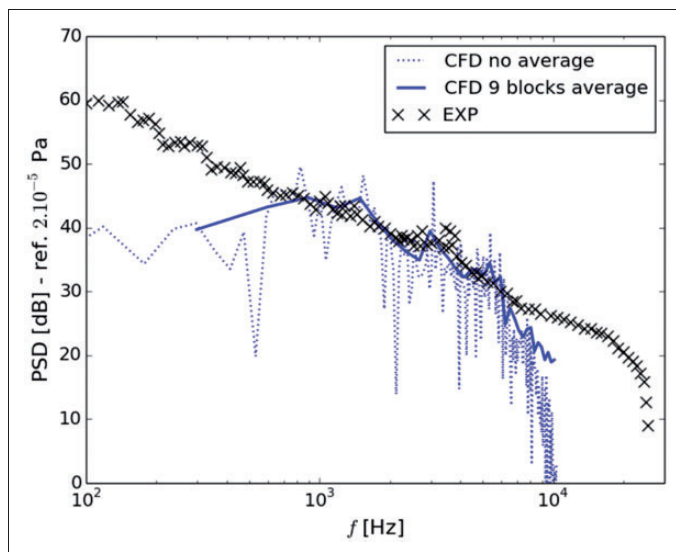
Figure 13. Sound power spectral density, at 2 m from the suction side of the airfoil, in the y-direction.

associate spectra are averaged). The averaged CFD spectrum is much smoother, and thus better adapted for comparison with the experiment, despite the rather large frequency step: nearly 300 Hz.

A remarkable agreement is observed between the experimental and numerical results, particularly in the central range (0.7 kHz, 7 kHz). As shown in the companion paper,[7] this range corresponds to the tip noise, which is addressed by the present simulation. At lower and higher frequencies, the experimental spectrum is dominated by the background noise and the trailing-edge noise induced by the boundary layer along the blade span. Such noise components are not included in the simulation, which uses LES only in the tip region. Consequently, the numerical spectrum is below the experimental one in the external frequency ranges. In the central frequency range (0.7 kHz, 7 kHz), the slope and the levels of the power spectral density are accurately predicted by the simulation. Two conclusions can be drawn from this result. First, this demonstrates the capabilities of the present numerical approach, relying on zonal RANS/LES, with a detailed LES description of the tip-flow. The simulation is able to reproduce the generation of broadband noise by the complex three-dimensional flow around the tip-clearance. Second, this confirms that the tip region essentially radiates in the central frequency range (0.7 kHz, 7 kHz). This is around the characteristic frequency of the TLV, as calculated above when analyzing the flow velocity spectra in Figure 12.

Conclusions

The three-dimensional tip leakage flow generated from the clearance between an isolated airfoil and a plate has been simulated. A zonal RANS/LES approach has been employed to describe with full LES the region of interest around the clearance, while a RANS description is used in the peripheral regions. The results have been compared with available experimental data.

The incoming end-plate boundary layer has a thickness similar to the tip-gap, and it is thus expected to influence the flow in the airfoil tip region. The development of this boundary layer is simulated with full LES over a limited width, and the comparisons with the measurements at three axial positions are fairly good.

The description of the jet in the simulation accounts for the deviation of the jet and its effect on the airfoil loading. Consequently, the mean pressure distribution around the airfoil is in good agreement with the experiment. In the tip-region, compared to the pressure coefficient at mid-span, the loading is reduced and a low-pressure hump is observed on the suction-side.

The TLV is intense, with mean cross-stream velocities of around U_0 downstream of the airfoil. The position of its center and its width have been quantified with the help of specific functions (Γ_1 and Γ_2). Again, a good agreement is observed with the experimental data. The artificial diffusion is moderate. The results on the fluctuating velocity confirm this.

Finally, the spectral content has been analyzed. In the tip region, around the trailing edge, a good agreement has been observed between the simulation and the experiment. The contribution of the TLV is located around 3 kHz, according to dimensional analysis. The far-field pressure has also been computed, using an acoustic analogy with some simplifications. A remarkable agreement is achieved with the experiment in the central range of frequencies (0.7 kHz, 7 kHz). It confirms the experimental suggestion that this range of frequencies is associated with the tip-flow noise.

Declaration of conflicting interests

Funding

References

1. Lakshminarayana B. *Fluid dynamics and heat transfer of Turbomachinery*. Hoboken, NJ: John Wiley and Sons, Inc, 1996.
2. Storer JA and Cumpsty NA. Tip leakage flow in axial compressors. *J Turbomach* 1991; 113: 252–259.
3. Hah C. *Large eddy simulation of transonic flow field in NASA Rotor 37*. Cleveland, OH: NASA, 2009. TM-2009-215627.
4. You D, Wang M, Moin P, et al. Large-eddy simulation analysis of mechanisms for viscous losses in a turbomachinery tip-clearance flow. *J Fluid Mech* 2007; 586: 177–204.
5. You D, Wang M, Moin P, et al. Vortex dynamics and low-pressure fluctuations in the tip-clearance flow. *J Fluids Eng* 2007; 129: 1002.
6. Boudet J, Cahuzac A, Kausche P, et al. Zonal large-eddy simulation of a fan tip-clearance flow, with evidence of vortex wandering. *J Turbomach* 2015; 137: 061001-061001-9.
7. Jacob MC, Jondeau E and Li B. Time resolved PIV measurements of a tip leakage flow. *Int J Aeroacoust* 2016.

8. Jacob MC, Grilliat J, Camussi R, et al. Aeroacoustic investigation of a single airfoil tip leakage flow. *Int J Aeroacoust* 2010; 9: 253–272.

9. Moreau S, Henner M, Iaccarino G, et al. Analysis of flow conditions in freejet experiments for studying airfoil self-noise. *AIAA J* 2003; 41: 1895–1905.

10. Winkler J, Moreau S and Carolus T. Airfoil trailing-edge blowing: broadband noise prediction from large-eddy simulation. *AIAA J* 2012; 50: 294–303.

11. Lévêque E, Toschi F, Shao L, et al. Shear-improved Smagorinsky model for large-eddy simulation of wall-bounded turbulent flows. *J Fluid Mech* 2007; 570: 491–502.

12. Wilcox DC. Reassessment of the scale-determining equation for advanced turbulence models. *AIAA J* 1988; 26: 1299–1310.

13. Boudet J, Monier J-F and Gao F. Implementation of a roughness element to trip transition in large-eddy simulation. *J Therm Sci* 2015; 24: 30–36.

14. Jameson A. Transonic airfoil calculations using the Euler equations. *Numerical methods in aeronautical fluid dynamics, vol. 1*. London: Academic Press, 1982, pp.289–308.

15. Ffowcs-Williams JE and Hawkings DL. Sound generated by turbulence and surfaces in arbitrary motion. *Philos Transact Royal Soc* 1969; A264: 321–342.

16. Casalino D. An advanced time approach for acoustic analogy predictions. *J Sound Vibrat* 2003; 261: 583–612.

17. Jacob MC, Dragna D, Cahuzac A, et al. Toward hybrid CAA with ground effects. *Int J Aeroacoust* 2014; 13: 235–260.

18. De Graaff DB and Eaton JK. Reynolds-number scaling of the flat-plate turbulent boundary layer. *J Fluid Mech* 2000; 422: 319–346.

19. Boudet J, Grilliat J, Caro J, et al. Combined experimental/computational study of tip clearance flow and acoustics. In: *8th European turbomachinery conference (ETC)*, Graz, Austria, 23–27 March 2009, pp.735–748.

20. Graftieaux L, Michard M and Grosjean N. Combining PIV, POD and vortex identification algorithms for the study of unsteady turbulent swirling flows. *Meas Sci Technol* 2001; 12: 1422–1429.

Appendix

Notation

c	chord length
C_p	mean pressure coefficient
EXP	experiment
h	tip-gap height
U_0	free-stream inflow velocity
V, W	mean velocity y- and z- components
v', w'	rms fluctuating velocity y- and z- components
x_{LE}	leading-edge abscissa
x, y, z	coordinates (see Figure 1)
β	zonal coefficient
Γ_1, Γ_2	vortex identification functions
μ_{mod}	global eddy viscosity
μ_{sgs}	LES subgrid-scale viscosity
μ_t	RANS turbulent viscosity
θ	angle of attack